Published in final edited form as:

Nat Immunol. 2019 November ; 20(11): 1506–1516. doi:10.1038/s41590-019-0505-z.

Mechanosensing by Peyer's patch stroma regulates lymphocyte migration and mucosal antibody responses

Jonathan E. Chang[1,2], **Matthew B. Buechler**[3], **Elise Gressier**[2], **Shannon J. Turley**[3,*], **Michael C. Carroll**[1,4,*]

[1]Division of Medical Sciences, Harvard Medical School, Boston, MA 02115, USA;

[2]Program in Cellular and Molecular Medicine, Children's Hospital, Boston, MA, 02215;

[3]Department of Cancer Immunology, Genentech, South San Francisco, CA 94080, USA

[4]Department of Pediatrics, Harvard Medical School, Boston, MA 02115, USA;

SUMMARY

Fibroblastic reticular cells (FRCs) and their specialized collagen fibers termed "conduits" form fundamental structural units supporting lymphoid tissues. In Lymph Nodes, conduits are known to transport interstitial fluid and small molecules from afferent lymphatics into the nodal parenchyma. However, the immunological contributions of conduit function have remained elusive. Here, we report that intestinal Peyer's patches (PPs) contain a specialized conduit system that directs the flow of water absorbed across the intestinal epithelium. Notably, PP FRCs responded to conduit fluid flow via the mechanosensitive ion channel Piezo1. Disruption of fluid flow or genetic deficiency of *Piezo1* on CCL19-expressing stroma led to profound structural alterations in perivascular FRCs and associated high endothelial venules. This in turn impaired lymphocyte entry into PPs and initiation of mucosal antibody responses. These results identify a critical role for conduit-mediated fluid flow in the maintenance of PP homeostasis and mucosal immunity.

Keywords

Peyer's patch; conduit; fluid flow; fibroblastic reticular cell; high endothelial venule; Piezo1; mechanosensation

*Correspondence M.C.C. (michael.carroll@childrens.harvard.edu) or S.J.T. (turley.shannon@gene.com).

Author Contributions

J.E.C designed and performed experiments, analyzed results, and wrote the manuscript; M.B.B. performed experiments, analyzed results, and contributed to the writing of the manuscript; E.G. performed experiments and analyzed results; M.C.C. and S.J.T designed and supervised the study and contributed to the writing of the manuscript.

Declarations of Interests

S.J.T. and M.B.B are employed by Genentech.

INTRODUCTION

Fibroblastic reticular cells (FRCs) provide the architectural framework supporting lymphoid tissues. In lymph nodes (LNs), FRCs deposit and ensheathe organized bundles of collagen fibers to form an intricate network extending from the subcapsular sinus to high endothelial venules (HEVs) and efferent lymphatics[1,2]. The anatomy of these structures allows for two functionally distinct compartments. The reticular network surface, comprised of interconnected FRC cell bodies, facilitates leukocyte attachment, cellular interactions and directional migration of leukocytes within the LN parenchyma, and is essential for lymphocyte homeostasis and the initiation of adaptive immune responses[3–8]. In contrast, the inner collagen core of the reticular network has been described as a conduit network, directing flow of lymph from the sinus into the LN parenchyma[1]. However, the functional and biological relevance of this latter aspect of the reticular network is less well established.

LN conduits have thus been proposed to function as an efficient and rapid pathway for transport of immunologically important soluble mediators from upstream tissues. Multiple reports have now demonstrated that lymph-borne antigen rapidly enters the LN conduit network where it can be directly sampled by resident dendritic cells (DCs) and follicular B cells through gaps in the FRC sheath[9–11]. Likewise, soluble chemokines are rapidly delivered via the conduit network to the ablumenal surface of the HEV, whereupon these molecules are transcytosed and decorate the vascular lumen[12–14]. This process leads to an increase in leukocyte homing. This latter example has led to a predicted model in which conduits facilitate a form of “remote control” wherein soluble mediators from upstream tissues can prime the LN for initiation of adaptive immune responses[14].

That FRC conduits mediate rapid and selective transport of soluble, small molecular weight material is a widely accepted concept. However, the necessity for conduit-mediated molecular and fluid transport for either LN homeostasis or initiation of adaptive immune responses has not been experimentally addressed. To date, no models exist in which to interrogate lymph node function in the absence of conduits. Nor have any physiological means of altering afferent lymph flow been developed, though surgical manipulation of upstream lymphatics has been reported[15–17]. Interestingly, LNs that have been surgically deprived of afferent lymph have been reported to exhibit a gradual “flattening” of the HEV, loss of glycam1 expression on the vascular endothelium, and a corresponding decrease in lymphocyte immigration. However, the specific contribution of conduit-mediated lymph flow to this phenomenon cannot be ascertained, as surgical deprivation of afferent lymph additionally impacts cellular migration of antigen-experienced DCs from upstream tissues.

Here we identify and describe FRC conduit networks in the intestinal Peyer’s patches (PPs). Unlike lymph nodes, PPs lack a conventional source of afferent lymph that would normally contribute fluid flow through the conduit network. Instead, PPs are located at the interface of the intestinal lumen and directly sample lumenal contents as opposed to lymph-borne materials. As with other regions of the intestine, the PP dome is lined with an absorptive epithelium that facilitates fluid transport through the establishment of local osmotic gradients. Here, we demonstrate that fluid absorbed in this manner enters a network of conduits that conduct the flow of fluid throughout the PP follicle and interfollicular regions.

Additionally, we provide evidence that prolonged disruption of fluid flow through PP conduits, or loss of FRC responsiveness to conduit flow via the mechanosensitive ion channel Piezo1, led to profound alterations to homeostatic lymphocyte recruitment to the PP and a reduced capacity to mount mucosal antibody immune responses.

RESULTS

PP conduits direct flow of absorbed lumenal fluid

Despite lacking a conventional source of afferent lymph flow, characterization of stromal components in the small intestinal PP reveals that these lymphoid organs are supported by an intricate network of collagen-rich reticular fibers, structurally similar to the conduit network found in lymph nodes (Fig. 1). These fibers extend from the subepithelial dome and project into both the B cell follicle and interfollicular regions. Scanning electron micrographs of alkali-water macerated PPs reveal that these reticular fibers emerge directly from the disorganized meshwork of collagen overlying the PP dome and eventually terminate directly along the blood vasculature (Fig. 1a). As with LN conduits, PP reticular fibers are ensheathed by a basement membrane and an interconnected network of FRCs, identified by expression of perlecan and podoplanin (PDPN), respectively (Fig. 1b,c).

A functional hallmark of LN FRC conduits is the ability to direct lymph flow from the lymph node sinus into the dense parenchyma of the cortex and paracortex, additionally facilitating delivery of soluble signaling molecules and antigen. The PP conduit network appears to perform a similar function, though drawing in fluid absorbed from the intestinal lumen in place of afferent lymph. Fluid uptake through PP conduits is identifiable through oral administration of soluble fluorescein isothiocyanate (FITC). Within two hours of gavage, FITC was detectable throughout the PP and selectively localized within the collagen-rich core of the conduit network (Fig. 1d).

High-magnification confocal imaging additionally confirmed that FITC-bearing conduits interface with blood vessels in the interfolliclular region of the PP (Fig. 1e). Moreover, FITC signal is detectable along the blood vessel wall, suggesting a path of directional fluid flow from the intestinal lumen to PP vasculature mediated by the PP conduit network. Together, these data demonstrate a functional reticular network of conduits supporting the intestinal PP. These conduits exhibit physical characteristics similar to those previously described in LNs, but uniquely function to facilitate fluid flow originating from the overlying intestinal epithelium as opposed to afferent lymph.

Perturbation of intestinal fluid absorption disrupts PP conduit flow

PP conduit flow appears uniquely dependent on fluid absorption across the intestinal epithelium, a process that is tightly regulated by maintenance of local osmotic gradients though ion transport (Fig. 2a). The functional consequences of perturbed conduit fluid flow in the PP can thus theoretically be addressed by means of blocking fluid absorption. Here, disrupted fluid absorption was achieved by two mechanistically distinct treatments – first by administration of a 10% solution of a high molecular weight polyethylene glycol (PEG) in drinking water, and secondly by oral gavage with amiloride hydrochloride. PEG is a non-

absorbable, non-metabolized osmotically active substance that increases the osmolarity of ingested fluid and promotes its retention in the intestinal lumen (Fig. 2b). By contrast, amiloride selectively disrupts the function of epithelial Na^+/H^+ exchangers, thereby preventing the establishment of sufficient osmotic gradients for directional water transport (Fig. 2c). Both models of disrupted fluid absorption were found to restrict fluid uptake into PP conduits, as visualized by uptake of soluble FITC after gavage (Fig. 2d–f). Under these conditions, we are thus able to examine the state of PP structure and function in the absence of conduit-mediated fluid flow.

Impaired fluid absorption disrupts HEV structure

Extended treatment of mice with PEG in drinking water for a period of up to 3 days does not result in gross changes to the overall architecture or total numbers of FRCs (Supplementary Fig. 1a), suggesting that fluid flow is not necessary for the maintenance of the FRC network itself. However, treatment with PEG for periods beyond one week resulted in a specific decrease in blood endothelial cell (BEC) numbers, including ECs of the PP HEV, identified by expression of mucosal addressin cell adhesion molecule 1 (MAdCAM1) (Supplementary Fig. 1b).

Changes to HEV EC cell numbers is preceded by a striking alteration in HEV structure. An intact PP HEV is structurally comprised of MAdCAM-expressing endothelium closely encircled by a ring of perivascular FRCs (Fig. 3a,c). Confocal imaging of the PP HEV following a 3-day treatment period with PEG revealed an apparent disruption in the normally continuous perivascular FRC ring and a quantifiable decrease in contact points between perivascular FRCs and HEV ECs (Fig. 3a). These structural alterations are also apparent by high-magnification transmission electron microscopy (TEM) of the PP HEV, which show distinct points of separation between the HEV ECs and surrounding basement membrane (Fig. 3b). Interestingly, these images additionally revealed an apparent dearth of leukocyte interactions with the vascular endothelium, as few cells were found either attached to the HEV lumen or within HEV pockets. This latter observation suggests a potential functional deficiency in HEV-mediated leukocyte immigration corresponding to perturbations in HEV structural integrity. In total, these data suggest that absence of directional conduit flow disrupts alignment of perivascular FRCs along the HEV (Fig. 3c).

Impaired fluid absorption disrupts lymphocyte recruitment

HEVs are the main port of entry for naive recirculating lymphocytes to lymphoid organs. Concurrent with the observed PEG-induced changes to HEV structure was a significant decrease in naïve lymphocyte recruitment to PPs. Adoptive transfer of splenocytes to either PEG or amiloride-treated recipient mice revealed a significant reduction in lymphocyte accumulation in PPs one hour after transfer relative to untreated control recipients (Fig. 4a). In contrast to PPs, recruitment of transferred lymphocytes to mesenteric LN (MLN), inguinal LN (ILN) and spleen remained normal. Additionally, equal ratio co-transfer of lymphocytes from control and PEG-treated donors to untreated recipients revealed no lymphocyte-intrinsic deficiency in homing to PPs (Fig. 4b). Rather, the defect in lymphocyte homing originates from the PP tissue environment itself.

Confocal imaging likewise revealed significantly fewer total lymphocytes accumulating within the PPs of PEG-treated recipients. Notably, these data also revealed a quantifiable reduction in lymphocytes found to be in direct contact with an HEV (Fig. 4c). However, this change was proportional to the reduction in total immigrating lymphocytes. Together, this suggests that there may be a deficiency in the initial interaction between lymphocytes and HEVs, leading to fewer total immigrating lymphocytes, but that the subsequent stages of lymphocyte extravasation and motility within PP tissue is not negatively affected.

Inefficient lymphocyte homing to the PPs eventually culminated in a roughly 2–3-fold decrease in total lymphocyte cellularity within 3 days of disrupted intestinal fluid absorption (Fig. 4d). Both B and T lymphocytes were affected equally. (Supplementary Fig. 2a). Additionally, alteration to PP cellularity was limited to recirculating lymphocyte populations, as the numbers of resident myeloid cell subsets were similar to untreated controls (Supplementary Fig. 2b). Pre-treatment of mice with the S1PR1 agonist FTY720, which limits lymphocyte recirculation and promotes retention in lymphoid tissues, effectively reversed PEG- or amiloride-induced alterations to PPs (Supplementary Fig. 2c). These data further suggest that regular trafficking of recirculating lymphocyte populations through intestinal PPs are affected by prolonged disruption of fluid absorption.

Interestingly, while we have observed no changes to recruitment of adoptively transferred lymphocytes to lymph nodes, total cell numbers of the MLNs and ILNs increased within 3 days of PEG or amiloride treatment (Fig. 4d). Increases to LN cellularity may be secondary to the loss of efficient lymphocyte homing to the PPs, or alternatively may result from unexpected systemic alterations associated with PEG or amiloride treatments, such as dehydration. Restoring mice to normal drinking water following PEG treatment effectively reversed altered LN and PP cellularity within just 12 hours (Supplementary Fig. 3a). However, subcutaneous administration of fluids failed to rescue PEG or amiloride-induced alterations to cellularity (Supplementary Fig. 3b). These data suggest that altered PP and LN cellularity following blockade of fluid absorption is not a consequence of dehydration. Rather, the process of fluid uptake via the oral route appears to be necessary for maintaining normal patterns of lymphocyte migration and homeostasis.

Impaired lymphocyte rolling on the HEV

Lymphocyte ingress across HEVs to lymphoid tissues is a multistep process which involves first selectin-mediated capture and rolling along the vascular endothelium, followed by integrin- and chemokine-mediated firm arrest and transmigration through endothelial cell junctions. Intravital multiphoton imaging of PPs following adoptive transfer of labeled lymphocytes revealed a near complete absence of lymphocyte rolling events on the HEV lumen of mice treated with PEG or amiloride (Supplementary Video 1, 2). By contrast, several lymphocyte rolling and adhesion events were identifiable within the HEVs of control mice (Supplementary Video 3).

Lymphocyte rolling in intestinal PPs is largely mediated through interaction between MAdCAM1 expressed by HEV ECs, and either L-selectin or the integrin α4β7 on recirculating lymphocytes[18]. Similar to treatments with PEG or amiloride, intravenous administration of a MAdCAM1 blocking antibody eliminated lymphocyte rolling events on

the HEV(Supplementary Video 4). Moreover, anti-MAdCAM1 treatment limited short-term lymphocyte accumulation in the PPs but not LNs (Fig. 5a), and anti-MAdCAM1 blockade over the course of 3 days resulted in an overall decrease in PP lymphocyte cellularity that was comparable to that seen following PEG and amiloride treatment (Fig. 5b). Combining PEG and anti-MAdCAM treatments did not result in an additive decrease to either short-term accumulation of circulating lymphocytes or overall cellularity in the PP (Fig. 5a,b). As such, we consider the possibility that these treatments are mechanistically redundant.

Despite noticeable changes to HEV structure following a three-day treatment with PEG, RNAseq analysis of flow cytometry-sorted HEV ECs and FRCs at this time point revealed few significant alterations in transcriptional profile. Notably, HEV EC expression of genes encoding key adhesion molecules involved in lymphocyte capture and recruitment, including MAdCAM1, was not significantly altered (Fig. 5c). Likewise, PP FRCs, which direct lymphocyte migration across HEVs, showed no significant alteration in transcript abundance for any known chemotactic signal involved in lymphocyte homing to the PP, including *Ccl19*, *Ccl21*, *Cxcl12*, and *Cxcl13* (data not shown).

While transcriptional expression of *Madcam1* appears unaffected by altered PP conduit flow, there was a striking difference in the amount of MAdCAM1 protein exposed on the luminal surface of HEVs. Lumenally exposed MAdCAM was specifically visualized by a short pulse of anti-MAdCAM1 (MAdCAM 488) delivered intravenously to control and PEG-treated animals. Significantly less *in vivo* labeling with anti-MAdCAM1 was observed in PEG-treated animals relative to control (Fig. 5d). Quantification of the percentage of lumenally exposed MAdCAM1 was performed by comparing *in vivo* labeled anti-MAdCAM1 (MAdCAM 488) signal to total anti-MAdCAM1 (MAdCAM-PE, visualized by post-fix staining). Under normal conditions, nearly all MAdCAM1 was exposed on the lumenal surface of HEVs. By contrast, this frequency drops to roughly 60% following PEG treatment (Fig. 5e). These data suggest that localization of MAdCAM1 protein, but not transcriptional expression, is altered in the absence of conduit fluid flow.

Blockade of fluid absorption impairs mucosal antibody responses

Access of lymph-borne material to the conduit network of lymph nodes is restricted to soluble molecules below a molecular weight cutoff of roughly 70 kDa[13]. Interestingly, this cutoff does not apply to molecules locally produced or directly injected into the LN itself, indicating that the physical properties of conduits themselves are not limiting[19]. Rather, size-selectivity in LN conduits is a property conferred by sinus-lining endothelial cells which contain transendothelial channels physically gated by fibrils formed by the glycoprotein PLVAP[20].

In contrast to LN conduits, the conduit network of PPs is not covered by these sinus-lining endothelial cells, but rather a monolayer of absorptive epithelium and microfold cells (M cells). The extent to which soluble antigen may access the PP conduit network, whether this access is size-selective, and the impact of this mode of antigen transport on mucosal immune responses has not previously been examined. To address this question, we co-administered a small 14 kDa hen egg lysozyme (HEL) antigen labeled with alexafluor 488 (HEL-488) and a large 250 kDa HEL labeled with phycoerythrin (HEL-PE) to the lumen of explanted

intestinal loops. Confocal imaging of the PPs revealed that 14 kDa HEL (HEL-488) rapidly penetrates the PP dome and tracks along the FRC conduit network, while HEL-PE primarily remained near the epithelial surface and appear to instead be carried into to PP follicle by myeloid cells (Fig. 6a). These data suggest that, as with LNs, conduit-mediated antigen transport within intestinal PPs appears to be limited to small molecular weight molecules.

To examine the immunological role of conduit-mediated antigen transport in PPs, PEG-treated and control mice were orally immunized with two nitrophenyl (NP)-haptenated protein antigens of differing molecular weights: 14 kDa NP-conjugated HEL (NP-HEL) and 150 kDa NP-conjugated chicken gamma globulin (NP-CGG). Given the size exclusivity of molecular transport through the PP conduit network, PEG-mediated blockade of fluid absorption and conduit flow should alter the route of intrafollicular transport for NP-HEL, while transport of the much large NP-CGG should be absent from PP conduits in both PEG-treated and control immunized mice. Following immunization, anti-NP fecal IgA titers were reduced in mice that had been concurrently treated with PEG to impair PP conduit flow (Fig. 6b). Interestingly, however, antibody responses to NP-HEL and NP-CGG were equally affected by treatment with PEG. Thus, while limitations in conduit flow can impact antigen-specific humoral responses in the PP, this is not necessarily a consequence of alterations in the mode of antigen transport.

Total fecal IgA titers in were likewise found to be lower in mice treated with PEG over the course of 2 weeks relative to control mice (Fig. 6c), and these mice exhibited a decrease in baseline germinal center (GC) cell activity (Fig. 6d). Under normal conditions, PPs exhibit continuous ongoing GC reactions regulated by an extensive network of follicular dendritic cells (FDCs). FRC interactions with FDCs have previously been noted in the context of antigen transport by LN conduits, and as PP conduits extend into the B cell zone of the PP, we considered the possibility that disrupted conduit flow may impact the FDC network or GC activity[9,21]. While GC activity was significantly decreased, the PP FDC network appeared structurally normal (Fig. 6e). Together, these data suggest a more general decrease in immune responsiveness to mucosal antigen when conduit flow is disrupted.

We speculate that this reduction may be a direct consequence of impaired homeostatic recruitment of naive lymphocytes to the PP following loss of conduit flow to the HEV. As previously established, anti-MAdCAM treatment directly impacts lymphocyte recruitment to the PP in a manner similar to PEG or amiloride treatment, but does so without any additional effects that might be associated with perturbed fluid absorption. We thus tested antigen-specific antibody responses in mice treated with anti-MAdCAM1 blockade during oral immunization. Under these conditions, mice exhibited fewer NP-specific B cells in the intestinal lamina propria (Fig. 6f,g), as well as a reduction in anti-NP IgA titers relative to control animals (Fig. 6h). Moreover, this reduction in antibody response was similar to that seen in mice immunized during PEG treatment. In total, these data suggest the amplitude of PP-derived mucosal immune responses is affected by the state of PP lymphocyte cellularity.

Piezo1 confers responsiveness to conduit flow in PP FRCs

Mechanical cues associated with directional fluid flow may be necessary for proper orientation of the HEV and surrounding perivascular network of FRCs. Previous reports

have demonstrated that vascular integrity may depend on expression of the mechanosensitive ion channel Piezo1 by endothelial cells, which confers morphological responsiveness to the sheer force exerted by vascular flow[22,23]. While PP conduits terminate at the ablumenal surface of HEVs, disrupted conduit-mediated fluid flow is unlikely to appreciably alter the rate of vascular flow or EC responsiveness. However, we find that FRCs likewise express *Piezo1* transcript, though at lower abundance than HEV ECs, and thus we examined the possibility that FRCsmay be similarly responsive to conduit-mediated fluid flow via Piezo1 signaling (Supplementary Fig. 4a).

Conditional Piezo1-deficient mice were generated by crossing mice expressing Cre recombinase directed by the *Ccl19* promoter (*Ccl19*cre) with mice expressing homozygous *lox*P sites around exons 20–23 of *Piezo1* (*Piezo1*$^{fl/fl}$); hereafter referred to as *Ccl19*-P1cKO (Supplementary Fig. 4b). Importantly, specificity of cre recombinase activity was tracked by alternatively crossing *Ccl19cre* mice with a *ROSA26*-eYFP reporter mouse and found to be largely restricted to PDPN-expressing stromal cells, with almost no expression in either LECs or BECs (Supplementary Fig. 4c). In contrast to the LN, a significantly smaller proportion of PDPN^{+}CD31^{-} cells isolated from PPs exhibit *Ccl19* reporter activity. However, these cells readily expand in culture and exhibit typical FRC morphology, and transcriptional expression of *Piezo1* was significantly ablated in culture-expanded FRCs isolated from Ccl19-P1cKO mice (Supplementary Fig. 4d,e).

Confocal imaging of PPs from these mice exhibited eYFP signal localized to PDPN^{+} FRCs surrounding the PP follicle and interfollicular region (Supplementary Fig. 5a). Additionally, we found clear reporter expression in FRCs surrounding the HEV, but no expression in HEV ECs (Supplementary Fig. 5b). By contrast, minimal eYFP signal was found within RANKL^{+} marginal reticular cells (MRCs) located in the subepithelial dome. Previous reports have suggested that FDCs may express low levels of Ccl19 and have demonstrated variable levels of Ccl19cre activity within the PP FDC network[24,25]. Here, we find that while the majority of the FDC network, identified as complement receptor-positive (CR1/CR2^{+}), were negative for reporter expression, a small subset of FDCs near the FRC/FDC interface may in fact be positive for eYFP expression, and thus cannot rule out the possibility that FDCs may also be partially targeted in these mice.

LNs and PPs develop normally in these mice, and the stromal cell composition was largely unchanged relative to *Ccl19*cre^{-}Piezo1$^{fl/fl}$ (wild-type) controls (Supplementary Fig. 6a). However, as with PEG-treated animals, we found that conditional ablation of *Piezo1* resulted in visible structural aberrations of the HEV-associated perivascular FRCs(Fig. 7a). Additionally, expression of MAdCAM1 exposed on the lumenal surface of the HEV endothelium was found to be significantly reduced in *Ccl19*-P1cKO mice relative to controls, suggesting a potential link between HEV polarization and Piezo1-mediated sensation of conduit fluid flow in HEV-supporting FRCs (Fig. 7b). In contrast to the HEV, LYVE1^{+} efferent lymphatics, along with the FRCs that interface with these vessels, appeared structurally normal in both PEG-treated and *Ccl19*-P1cKO mice (Supplementary Fig. 6b).

As with PEG-treated mice, alterations to HEV structure in *Ccl19*-P1cKO mice were associated with reductions in lymphocyte recruitment to the PPs in *Ccl19*-P1cKO as well as a cumulative decrease in overall lymphocyte cellularity (Fig. 7c,d). This perturbation in lymphocyte recruitment affected both naive circulating B cell and T cell populations (Supplementary Fig. 6c). Interestingly, *Ccl19*-P1cKO mice also exhibited increases to lymph node cellularity in a manner similar to that observed following PEG or amiloride treatment, despite LN FRCs expressing similar baseline levels of *Piezo1* transcript to PP FRCs (Fig. 7c,d; Supplementary Fig. 6d). This suggests that LN FRCs may not rely on Piezo1 to support homeostatic maintenance or accumulation of lymphocytes to LNs. Finally, oral immunization of *Ccl19*-P1cKO mice against NP-CGG resulted in less potent mucosal IgA responses as compared to wild-type controls. Fewer NP-specific B cells were present in the intestinal lamina propria (Fig. 7e,f), and NP-specific fecal IgA titers were significantly lower (Fig. 7g).

Cumulatively, these data suggest that mechanosensation of conduit-mediated fluid flow via Piezo1 contributes to the proper alignment of PP FRCs, particularly at the site of FRC-HEV interaction where conduits terminate along the vessel's ablumenal surface. Loss of Piezo1 signaling within *Ccl19*-expressing stroma of PPs results in structural aberrations at HEVs, impaired recruitment and accumulation of lymphocytes to PPs, and a reduced capacity to establish mucosal antibody response against antigen.

DISCUSSION

Various descriptions of the reticular network functioning as a conduit for the transport or distribution of soluble material have been reported over the last several decades[1,26–28], leading to speculation of immunologically important roles for conduit-mediated transport of chemokines and antigen[9–14]. However, exploration of LN conduit networks thus far has been largely restricted to interpretation of *in situ* imaging, and thus our understanding of conduit networks remains purely descriptive. It has proven far more challenging experimentally examine the biological importance of conduits and conduit-mediated fluid transport.

To date, the only means of effectively depriving a LN of conduit flow relies on the surgical ligation of afferent lymph vessels – a process which not only deprives LNs of lymph flow and lymph-borne soluble mediators, but also of tissue-derived migrating dendritic cells (DCs) as well[15–17]. Thus, the specific contributions of disrupted conduit flow cannot be definitively established by this experimental approach. Here, we alternatively sought to gather insight into the biological importance of fluid flow through a reticular conduit network supporting intestinal Peyer's patches, which is uniquely linked with the process of epithelial fluid absorption and thus more experimentally pliable than that of LN conduits. Following prolonged disruption of intestinal fluid absorption, we find that PP HEV structure is perturbed and lymphocyte recruitment and cellularity decrease substantially. While disruption of fluid absorption negatively impacts lymphocyte recruitment to PPs, we also note a surprising increase in cellularity of LNs. This increased LN cellularity may result from a redistribution of circulating lymphocytes, which might otherwise accumulate in the PP.

Interestingly, these HEVs also exhibited a decrease in the display of MAdCAM1 at the vascular lumen, but few alterations to transcriptional profile, suggesting an alteration to endothelial polarization rather than impaired HEV differentiation. FRCs, which line the conduit network and interface with the HEV, likewise exhibit few transcriptional alterations. However, evidence that both FRCs and HEVs may be functionally and morphologically affected by the mechanical force exerted by fluid flow have been previously reported[22,23,29]. Mechanosensation of vascular fluid flow by ECs, for instance, has been attributed to expression of Piezo1. We examined here the impact of Piezo1 signaling specifically in Ccl19-expressing stromal cells, which consists primarily of FRCs and a small subset of FDCs, to determine whether these cells similarly sense and respond to conduit-mediated directional fluid flow. Indeed, we find many alterations to PP homeostasis that closely resemble the effects of PEG or amiloride-induced perturbations in fluid absorption and thus suggest that expression of Piezo1 by PP FRCs confers responsiveness to conduit-mediated fluid flow in the PP.

These alterations to lymphocyte trafficking demonstrate the functional importance of conduit networks for the homeostatic maintenance of lymphoid tissues. However, we have additionally demonstrated that blockade of fluid absorption and directional conduit flow negatively impacts the amplitude of antigen-specific mucosal IgA responses. A role for conduit-mediated transport of IgM antibodies secreted locally in the lymph node has recently been demonstrated, suggesting that conduit transport may be key contributors to antibody responses[19]. Conduits in the PP may likewise contribute to the export of locally produced antibody. However, we additionally observed a decrease in PP GC activity, as well as decreases in the number of antigen specific B cells in mice orally immunized against NP-haptinated protein. These data suggest that loss of conduit flow impacts the initiation of B cell responses as well.

The mechanistic link between PP conduit flow and initiation of B cell responses is not entirely clear. It has also been proposed that conduits may contribute to immune responses by providing an alternative route for the transport of antigen. However, we found no evidence that the size of antigen or its transport through PP conduits impacts the resulting immunological response. It is additionally possible that alteration to the FDC network, which may intersect with the conduit network, may be a contributing factor to altered mucosal responses following impaired conduit flow[21]. While we have not observed any clear alterations to the size or structure of the FDC network, the function of FDCs in this context may warrant future investigation.

An alternative explanation for decreases in IgA responses following blockade of fluid absorption is that impaired lymphocyte recruitment to the PP restricts the pool of naive lymphocytes locally available to respond to antigen. Previous studies quantifying the primary immune B cell and T cell precursor populations have demonstrated a striking correlation between the size of an antigen-reactive precursor population and the amplitude of primary immune responses to cognate antigen upon immunization - the larger the naive precursor population, the more robust the primary adaptive immune response[30–33]. By extension, the total number of antigen-reactive naive B cells available in the PP at the time of immunization may directly influence the amplitude of resultant immune responses. In line

with this concept, the effects of impaired fluid absorption on mucosal antibody responses can be largely recapitulated in mice treated systemically with anti-MAdCAM or in Ccl19-P1cKO mice, wherein lymphocyte cellularity of the PP is reduced, but fluid absorption and conduit flow are normal. The clear shift in lymphocyte population distribution away from the PPs and towards LNs might therefore broadly impact the nature of immune responses an individual may be prepared to elicit.

Cumulatively, we have shown that the PP conduit network plays an integral role in supporting PP immune homeostasis. The loss of conduit flow not only impacted lymphocyte recruitment and PP cellularity, but also culminated in decreased capacity to mount mucosal immune responses. Due to the unique link between PP conduit flow and intestinal fluid absorption, we anticipate that these processes may be particularly relevant when considering conditions characterized by fluid malabsorption such as inflammatory or infectious diarrheal diseases and chronic laxative use. Ultimately, the contribution of fluid absorption and PP conduit fluid flow within the greater context of mucosal health and disease should be a topic a great interest for future investigation.

METHODS

Mice.

Experiments were performed in C57BL/6 mice unless otherwise indicated. C57Bl/6J mice, *Villin*Cre mice (021504), and *Piezo1*$^{fl/fl}$ mice[34] (029213) were purchased from Jackson Laboratories. *Rosa26*-SSB-BFP mice were generated in the laboratory and previously described[35]. *Villin*Cre mice were crossed to the Rosa26-SSB-BFP line to generate *Villin*Cre-SSB-BFP mice. *Ccl19*Cre mice were obtained from B. Ludewig (Kantonsspital St. Gallen, Switzerland) and have been previously described[36]. Ccl19-P1cKO mice were generated by crossing *Ccl19*cre$^{+/-}$ heterozygous mice with Piezo1$^{fl/fl}$ homozygous mice twice to generate *Ccl19*cre$^{+/-}$*Piezo1*$^{fl/fl}$ breeders. These mice were then crossed with *Piezo1*$^{fl/fl}$ mice to generate either *Ccl19*cre$^{+/-}$*Piezo1*$^{fl/fl}$ (Ccl19-P1cKO) or *Ccl19*cre$^{-/-}$*Piezo1*$^{fl/fl}$ (WT) offspring for experimentation. All resulting offspring are of mixed C57BL/6N and C57BL/6J background. Cre negative littermates were used as WT controls in each experiment. Mice were maintained under specific pathogen-free conditions in accordance with institutional and National Institute of Health guidelines and used at 6–8 weeks of age. For each of the experiments performed, age-matched mice of both sexes were analyzed. Experiments were approved by the Boston Children's Hospital and Harvard Medical School institutional animal use and care committee in accordance with NIH guidelines for the humane treatment of animals

Antibodies.

The following antibodies were used: αCD45 (30-F11), αCD31 (390), αPDPN (8.1.1), αMadCAM-1 (MECA-367), αB220 (RA3–6B2), αCD11b (M1/70), αCD11c (N418), αCD8a (53–6.7), αEpCAM (G8.8), αCD3e (145–2C11), αTER119 (TER119), αCR1/CR2 (7E9), αGL7 (GL7), and αCD38 (90) from BioLegend, αPerlecan (A7L6) from ThermoFischer Scientific, αIgA (C10–3) from BDbioscience, αCol1 (Millipore sigma).

Disruption of fluid absorption.

Fluid absorption was disrupted by one of two treatments. *Polyethylene glycol (PEG):* PEG was administered to mice through *ad libitum* through drinking at a concentration of 10% (w/v) for a duration of up to 2 weeks, depending on experiment. *Amiloride Hydrochloride:* Mice were orally gavaged with amiloride (0.1mg/kg) once daily for up to 3 days, depending on experiment.

Immunohistochemistry and confocal microscopy.

Isolated tissues were fixed in 4% paraformaldhehyde (PFA) for 4 h and placed in 30% sucrose until saturation. Tissue was embedded in OCT medium (Optimal Cutting Temperature), frozen, and cut into 20 μm sections. Sections were stained and imaged using Inverted Olympus IX 81 confocal microscope.

Intravital imaging by multiphoton microscopy.

Mice are anesthetized by inhalation of isoflurane and maintained at physiological temperature with a closed-circuit heated water circulation system. A small loop of intestine is exposed from the anesthetized mouse and immobilized on a heated stage. CMFDA (5-chloromethylfluorescein diacetate)-labeled naive lymphocytes are adoptively transferred, and the blood vasculature is illuminated by intravenous injection with fluorescently labeled vascular-impermeable Qdots (Thermo Fisher Scientific, Q21031MP). Under these conditions, the exposed Peyer's patch can be imaged for a period of at least one hour. Imaging was performed on an Olympus BX 61 WI multiphoton microscope with a Spectra Physics MaiTai DSHP laser.

GC and FDC quantification.

PP tissue sections were stained for confocal microscopic analysis. Resulting images were analyzed using ImageJ software to identify the perimeter of the FDC network. MFI of $GL7^+$ staining within the FDC network was then quantified.

Enzymatic digestion of lymphoid organs.

Single cell suspensions of LN, PP, and spleen were prepared for analysis by flow cytometry. *Lymph nodes*: LNs were dissected and incubated at 37 °C in RPMI containing 0.1 mg/ml Dnase I (Invitrogen), 0.2 mg/ml Collagenase P (Roche) and 0.8 mg/ml Dispase (Roche) for 50–60 min, as previously described[37]. Cells were collected in medium containing 2% FBS and 5 mM EDTA every 15–20 min and replaced with fresh digestion medium. *Peyer's patches (PPs)*: Intestines were dissected and washed by lavage with ice cold PBS. PPs were removed from the intestine and washed in a solution 2 mM EDTA and 5% DTT in PBS for 20 min at 37°C to remove the epithelium. PPs were then enzymatically digested (as with the LN). *Spleen:* Lymphocyte were extracted from the spleen by mechanical disruption and passage through a 70-μm cell strainer. Red blood cells were lysed with ACK buffer before analysis by flow cytometry.

RNAseq Analysis.

For each mouse, 1,000 PP FRCs or HEV ECs were sorted into 5 μl/well of TCL (Qiagen #1031576) buffer containing 1% 2-mercaptoethanol. RNA was isolated using RNAClean XP beads (Agencourt A63987). Template switching, cDNA synthesis and cDNA amplification were adapted from previous studies[38]. Libraries were prepared using the Nextera kit (Illumina). Libraries were sequenced using an Illumina HiSeq yielding, on average, 27.5 million reads pairs per sample. RNA-sequencing data were analyzed using HTSeqGenie package in BioConductor[39] as follows: first, reads with low nucleotide qualities (70% of bases with quality <23) or rRNA and adapter contamination were removed. The reads that passed were then aligned to the reference genome GRCh37 using GSNAP[40]. 1.6 – 4.3 % reads were of low quality and were removed. The percentage rRNA contamination ranged from 1.16 – 4.64 %. These were also removed. Reads that were uniquely mapped were used for subsequent analysis. Gene expression levels were quantified as Reads Per Kilobase of exon model per Million mapped reads normalized by size factor (nRPKM), defined as number of reads aligning to a gene in a sample / (total number of uniquely mapped reads for that sample × gene length × size factor). Differential expression analysis was performed using voom/limma[41].

Tissue preparation for TEM.

Segments of intestine roughly 2-cm long and containing at least one PP were excised and tied at either end. The lumen of these intestinal “loops” were then filled with FGP fixative (2.5% paraformaldehyde, 5% glutaraldehyde, 0.06% picric acid in 0.2M cacodylate buffer), and the filled loops were then drop-fixed overnight in the same solution. Fixed sections were washed in 0.1M cacodylate buffer and post-fixed with 1% osmium tetroxide (OsO4)/1.5% potassium ferrocyanide (KFeCN6) for 1h, washed in water three times and incubated in 1% aqueous uranyl acetate for 1h followed by two washes in water and subsequent dehydration in grades of alcohol (10min each; 50%, 70%, 90%, 2× 10min 100%). The samples were then placed in propyleneoxide for 1h subsequently infiltrated overnight in a 1:1 mixture of propyleneoxide and TAAB Epon (Marivac Canada Inc.). The following day the samples were embedded in TAAB Epon and polymerized at 60°C for 48h. Ultrathin sections (about 60nm) were cut on a Reichert Ultracut-S microtome, placed onto copper grids, stained with uranyl acetate and lead citrate and examined on a JEOL 1200EX microscope. Images were recorded with an AMT 2k CCD camera.

Tissue preparation for SEM.

Samples were fixed for 1–2 days in FGP Fixative as was described for TEM. Fixed PPs were then subjected to alkali-water maceration by immersion in a 10% aqueous solution of NaOH for 5 days at 20°C. Samples were then rinsed twice in distilled water for 1 day each, until they became transparent. The alkali-water macerated specimens were then treated with 0.5–1% tannic acid solution for 2–5 h, washed in distilled water for 1 h, and immersed in 1% OsO_2 solution for several hours. The specimens were dehydrated in a series of graded concentrations of ethanol and transferred to isoamyl acetate. Samples were then briefly frozen in liquid nitrogen and cracked with a razor blade to expose the inside of the PP for imaging before immediately re-immersing in 100% ethanol. Specimens are then dried using

a Tousimis 931 GL critical-point dryer. The dried specimens were then affixed on aluminum stubs with adhesives, coated with platinum-palladium using an EMS 300T D dual head sputter coater, and examined by SEM on a Zeiss Ultra55 FESEM.

Conduit analysis.

Mice were gavage fed with 400 μl of FITC-saturated PBS solution 2–4 h before harvesting the intestine. To examine the effects of blockade of fluid absorption, mice were 1) gavage fed with 400 μl of FITC saturated PBS solution with 10% PEG, or 2) gavage fed with FITC in PBS 2 h following gavage treatment with amiloride (0.1mg/kg). The intestinal lumen was washed by lavage with 10 ml of ice cold PBS. Peyer's patches were then excised and fixed in 4% PFA. Fixed tissues were immersed in 30% sucrose for cryoprotection and then frozen in O.C.T. Thick 100 μm sections were cut using a cryostat. Sections were imaged by multiphoton microscopy.

Adoptive transfer of lymphocytes.

A single-cell suspension of naive lymphocytes was prepared from spleens from C57BL/6 donor mice and immediately labeled with CellTracker Green CMFDA dye (ThermoFisher Scientific C2925). Lymphocytes were adoptively transferred to either untreated control, PEG-treated, amiloride-treated recipient mice by retro-orbital injection in 50 μl of sterile saline. Alternatively, lymphocytes were adoptively transferred in sterile saline containing 20 μg of anti-MAdCAM1 antibody. For comparison of lymphocytes from untreated control and PEG-treated donor mice, donor splenocytes were similarly harvested and labeled, then mixed in a 1:1 ratio before adoptive transfer to recipient mice. For all experiments, mice were euthanized 1 h after adoptive transfer, and PPs and ILNs were harvested for analysis.

FTY720 treatments.

To prevent cell egress, mice were injected with 1 mg/kg FTY720 (Fingolimod, R&D) i.p. immediately prior to the start of treatment with PEG or amiloride. Mice received an additional dose of FTY720 at 48 h and were sacrificed for analysis at 72 h.

Antibody blockade of MAdCAM-1.

To block lymphocyte interactions with the PP HEV, mice were injected I.V. with 20 μg of anti-MAdCAM (MECA-367). For experiments examining short-term recruitment of adoptively transferred lymphocytes, mice were given a single injection simultaneous with cell adoptive transfer. For experiments examining long-term effects on PP cellularity and antibody response, mice were injected once daily with 20 μg.

In vivo labeling of MAdCAM-1.

Control or PEG-treated mice received 20ug of anti-MAdCAM1–488 by retro-orbital injection. Mice were euthanized 10 min after injection and perfused with ice cold 4% PFA. PPs were harvested and drop-fixed in PFA for an additional 4 h, immersed in 30% sucrose overnight, and frozen in OCT. Tissue sections were then stained with anti-MAdCAM1-PE and analyzed by confocal microscopy. Images were imported to FlowJo software, and pixel

intensity for either 488 or PE channels was assessed for each pixel. Data was quantified as % pixels positive in the 488 channel out of all stained pixels (488+PE).

Image quantification of HEV-associated lymphocytes.

Confocal imaging was performed on PPs harvested from mice following adoptive transfer of CMFDA labeled lymphocytes. Sections were counterstained with anti-MAdCAM to label HEVs. Masks of HEV staining were created from in ImageJ software and lymphocyte numbers within masks were quantified as lymphocytes associated with the HEV.

Image quantification of HEV-FRC contact points.

Confocal imaging was performed on PPs harvested from either B6 mice following treatment with PEG, or from *Ccl19*-P1cKO mice. Sections were stained with anti-MAdCAM to label HEVs and anti-PDPN to label FRCs. Image analysis was performed in ImageJ. Binary images of each channel (HEV and FRC) were generated by thresholding. A perimeter of the HEV was generated by dilating the HEV threshold image once, and then subtracting the original HEV threshold. Contact points were determined as all pixels in which the FRC-threshold image overlap with the HEV perimeter. Data is represented as (contact points)/(HEV perimeter).

Oral immunization and mucosal antibody responses.

For analysis of antigen-specific mucosal antibody responses, control (untreated) or PEG-treated animals received either NP-HEL (100 μg) or NP-CGG (20 μg) once daily by oral gavage for 2 weeks. Unimmunized controls received PBS once daily by oral gavage for the same duration. All mice were allowed to recover on normal drinking water for 3 days following the final immunization. Stool was collected for fecal IgA titers analysis. Intestinal tissue was harvested for enzymatic digestion and analysis by flow cytometry. Fecal IgA was extracted as follows: Fecal pellets were homogenized with a TissuLyser LT bead mill (Qiagen) in a solution of protease inhibitor cocktail in PBS for 10 min. Non-soluble fecal material was removed by two rounds of centrifugation at 4°C. Supernatant containing soluble fecal-IgA was reserved for analysis by ELISA, while the pellet was allowed to dry and subsequently weighed. Sample volume was normalized to fecal dry weight. ELISA analysis was performed through immobilization of NP-BSA on a high binding plate (Greiner Bio-One, 655081), addition of fecal-IgA preparation at 2-fold serial dilutions, and probing for specific binding of Goat polyclonal anti-IgA-AP (southern biotech) using standard alkaline phosphatase development. For analysis of total fecal IgA, high binding plates were coated with goat polyclonal anti-IgA capture antibody (Southern Biotech), followed by addition of fecal-IgA preparation, and probing for specific binding of rat anti-IgA-AP (11-44-2) by alkaline phosphatase development.

Analysis of NP-specific B cells.

Small intestines were harvested from mice following oral immunization against NP-CGG. PPs were removed and fat was carefully dissected away. The intestine was cut into 2–3-cm long segments and inverted using forceps. Intestinal segments were then washed twice in 2 mM EDTA and 5% DTT in PBS at 37°C for 20 min each to remove epithelium. The

remaining lamina propria was enzymatically digested at 37 °C in RPMI containing 0.1 mg/ml Dnase I (Invitrogen), 0.2 mg/ml Collagenase P (Roche) and 0.8 mg/ml Dispase (Roche) for 50–60 min. NP-specific B cells were then identified by incubation with NP-PE for 20 min on ice, then analyzed by flow cytometry.

Statistical analysis.

All averaged data is presented as +/− S.E.M. Statistical tests were performed using GraphPad Prism software. For experiments comparing two treatment groups, a two-tailed, unpaired Student's *t* test was performed. For comparison of three or more treatment groups, a one-way ANOVA was performed followed by Tukey's post hoc multiple comparison tests. Differences were considered to be statistically significant when $P < 0.05$. For graphs, data are shown as mean +/− SEM. Statistical significance is indicated with the following: * ($P \leq 0.05$), ** ($P \leq 0.01$), *** ($P \leq 0.005$). No statistical significance is indicated with "ns"

Data Availability.

The data that support the findings of this study are available from the corresponding author upon request. Microarrays are available on the Gene Expression Omnibus (GEO) database with the accession number GSE135612.

Supplementary Material

Refer to Web version on PubMed Central for supplementary material.

Acknowledgements

We thank the members of the Carroll Lab and Turley Lab for comments and suggestions on the study. We thank B. Ludewig (Kantonsspital St. Gallen, Switzerland) for providing *Ccl19*Cre mice. This study was funded in part by Genentech and by the US National Institutes of Health (F31 DK1055 to J.E.C.; R33 AI110164 and RO1 AI130307 to M.C.C.; RO1 DK074500 and R21 CA182598 to S.J.T.). We thank S. Jhunjhunwala and N. Lounsbury for management of sequencing files and data processing.

REFERENCES

1. Anderson AO & Anderson ND Studies on the structure and permeability of the microvasculature in normal rat lymph nodes. Am J Pathol 80, 387–418 (1975). [PubMed: 1163637]
2. Gretz JE, Anderson AO & Shaw S Cords, channels, corridors and conduits: critical architectural elements facilitating cell interactions in the lymph node cortex. Immunol Rev 156, 11–24 (1997). [PubMed: 9176696]
3. Bajenoff M et al. Stromal cell networks regulate lymphocyte entry, migration, and territoriality in lymph nodes. Immunity 25, 989–1001, doi:10.1016/j.immuni.2006.10.011 (2006). [PubMed: 17112751]
4. Cremasco V et al. B cell homeostasis and follicle confines are governed by fibroblastic reticular cells. Nature immunology 15, 973–981, doi:10.1038/ni.2965 (2014). [PubMed: 25151489]
5. Gunn MD et al. A B-cell-homing chemokine made in lymphoid follicles activates Burkitt's lymphoma receptor-1. Nature 391, 799–803, doi:10.1038/35876 (1998). [PubMed: 9486651]
6. Hase H et al. BAFF/BLyS can potentiate B-cell selection with the B-cell coreceptor complex. Blood 103, 2257–2265, doi:10.1182/blood-2003-08-2694 (2004). [PubMed: 14630796]
7. Link A et al. Fibroblastic reticular cells in lymph nodes regulate the homeostasis of naive T cells. Nature immunology 8, 1255–1265, doi:10.1038/ni1513 (2007). [PubMed: 17893676]

8. Luther SA, Tang HL, Hyman PL, Farr AG & Cyster JG Coexpression of the chemokines ELC and SLC by T zone stromal cells and deletion of the ELC gene in the plt/plt mouse. Proc Natl Acad Sci U S A 97, 12694–12699, doi:10.1073/pnas.97.23.12694 (2000). [PubMed: 11070085]
9. Roozendaal R et al. Conduits mediate transport of low-molecular-weight antigen to lymph node follicles. Immunity 30, 264–276, doi:10.1016/j.immuni.2008.12.014 (2009). [PubMed: 19185517]
10. Sainte-Marie G & Peng FS Diffusion of a lymph-carried antigen in the fiber network of the lymph node of the rat. Cell Tissue Res 245, 481–486 (1986). [PubMed: 3757012]
11. Sixt M et al. The conduit system transports soluble antigens from the afferent lymph to resident dendritic cells in the T cell area of the lymph node. Immunity 22, 19–29, doi:10.1016/j.immuni.2004.11.013 (2005). [PubMed: 15664156]
12. Baekkevold ES et al. The CCR7 ligand elc (CCL19) is transcytosed in high endothelial venules and mediates T cell recruitment. J Exp Med 193, 1105–1112 (2001). [PubMed: 11342595]
13. Gretz JE, Norbury CC, Anderson AO, Proudfoot AE & Shaw S Lymph-borne chemokines and other low molecular weight molecules reach high endothelial venules via specialized conduits while a functional barrier limits access to the lymphocyte microenvironments in lymph node cortex. J Exp Med 192, 1425–1440 (2000). [PubMed: 11085745]
14. Stein JV et al. The CC chemokine thymus-derived chemotactic agent 4 (TCA-4, secondary lymphoid tissue chemokine, 6Ckine, exodus-2) triggers lymphocyte function-associated antigen 1-mediated arrest of rolling T lymphocytes in peripheral lymph node high endothelial venules. J Exp Med 191, 61–76 (2000). [PubMed: 10620605]
15. Hendriks HR, Duijvestijn AM & Kraal G Rapid decrease in lymphocyte adherence to high endothelial venules in lymph nodes deprived of afferent lymphatic vessels. Eur J Immunol 17, 1691–1695, doi:10.1002/eji.1830171203 (1987). [PubMed: 3500859]
16. Hendriks HR & Eestermans IL Disappearance and reappearance of high endothelial venules and immigrating lymphocytes in lymph nodes deprived of afferent lymphatic vessels: a possible regulatory role of macrophages in lymphocyte migration. Eur J Immunol 13, 663–669, doi:10.1002/eji.1830130811 (1983). [PubMed: 6884423]
17. Mebius RE et al. Expression of GlyCAM-1, an endothelial ligand for L-selectin, is affected by afferent lymphatic flow. J Immunol 151, 6769–6776 (1993). [PubMed: 7505014]
18. Berg EL, McEvoy LM, Berlin C, Bargatze RF & Butcher EC L-selectin-mediated lymphocyte rolling on MAdCAM-1. Nature 366, 695–698, doi:10.1038/366695a0 (1993). [PubMed: 7505053]
19. Thierry GR et al. The conduit system exports locally secreted IgM from lymph nodes. J Exp Med 215, 2972–2983, doi:10.1084/jem.20180344 (2018). [PubMed: 30429248]
20. Rantakari P et al. The endothelial protein PLVAP in lymphatics controls the entry of lymphocytes and antigens into lymph nodes. Nature immunology 16, 386–396, doi:10.1038/ni.3101 (2015). [PubMed: 25665101]
21. Gonzalez SF et al. Trafficking of B cell antigen in lymph nodes. Annu Rev Immunol 29, 215–233, doi:10.1146/annurev-immunol-031210-101255 (2011). [PubMed: 21219172]
22. Li J et al. Piezo1 integration of vascular architecture with physiological force. Nature 515, 279–282, doi:10.1038/nature13701 (2014). [PubMed: 25119035]
23. Ranade SS et al. Piezo1, a mechanically activated ion channel, is required for vascular development in mice. Proc Natl Acad Sci U S A 111, 10347–10352, doi:10.1073/pnas.1409233111 (2014). [PubMed: 24958852]
24. Rodda LB, Bannard O, Ludewig B, Nagasawa T & Cyster JG Phenotypic and Morphological Properties of Germinal Center Dark Zone Cxcl12-Expressing Reticular Cells. J Immunol 195, 4781–4791, doi:10.4049/jimmunol.1501191 (2015). [PubMed: 26453751]
25. Rodda LB et al. Single-Cell RNA Sequencing of Lymph Node Stromal Cells Reveals Niche-Associated Heterogeneity. Immunity 48, 1014–1028 e1016, doi:10.1016/j.immuni.2018.04.006 (2018). [PubMed: 29752062]
26. Anderson AO & Shaw S T cell adhesion to endothelium: the FRC conduit system and other anatomic and molecular features which facilitate the adhesion cascade in lymph node. Semin Immunol 5, 271–282, doi:10.1006/smim.1993.1031 (1993). [PubMed: 8219105]

27. Gretz JE, Kaldjian EP, Anderson AO & Shaw S Sophisticated strategies for information encounter in the lymph node: the reticular network as a conduit of soluble information and a highway for cell traffic. J Immunol 157, 495–499 (1996). [PubMed: 8752893]
28. Moe RE Fine Structure of the Reticulum and Sinuses of Lymph Nodes. Am. J. Anat 110, 217–257 (1963).
29. Tomei AA, Siegert S, Britschgi MR, Luther SA & Swartz MA Fluid flow regulates stromal cell organization and CCL21 expression in a tissue-engineered lymph node microenvironment. J Immunol 183, 4273–4283, doi:10.4049/jimmunol.0900835 (2009). [PubMed: 19734211]
30. Abbott RK et al. Precursor Frequency and Affinity Determine B Cell Competitive Fitness in Germinal Centers, Tested with Germline-Targeting HIV Vaccine Immunogens. Immunity 48, 133–146 e136, doi:10.1016/j.immuni.2017.11.023 (2018). [PubMed: 29287996]
31. Jenkins MK & Moon JJ The role of naive T cell precursor frequency and recruitment in dictating immune response magnitude. J Immunol 188, 4135–4140, doi:10.4049/jimmunol.1102661 (2012). [PubMed: 22517866]
32. Moon JJ et al. Naive CD4(+) T cell frequency varies for different epitopes and predicts repertoire diversity and response magnitude. Immunity 27, 203–213, doi:10.1016/j.immuni.2007.07.007 (2007). [PubMed: 17707129]
33. Obar JJ, Khanna KM & Lefrancois L Endogenous naive CD8+ T cell precursor frequency regulates primary and memory responses to infection. Immunity 28, 859–869, doi:10.1016/j.immuni.2008.04.010 (2008). [PubMed: 18499487]
34. Cahalan SM et al. Piezo1 links mechanical forces to red blood cell volume. Elife 4, doi:10.7554/eLife.07370 (2015).
35. Degn SE, Alicot E & Carroll MC B cell tolerance to epidermal ribonuclear-associated neo-autoantigen in vivo. Clin Exp Immunol 191, 151–165, doi:10.1111/cei.13066 (2018). [PubMed: 28984923]
36. Chai Q et al. Maturation of lymph node fibroblastic reticular cells from myofibroblastic precursors is critical for antiviral immunity. Immunity 38, 1013–1024, doi:10.1016/j.immuni.2013.03.012 (2013). [PubMed: 23623380]
37. Fletcher AL et al. Reproducible isolation of lymph node stromal cells reveals site-dependent differences in fibroblastic reticular cells. Front Immunol 2, 35, doi:10.3389/fimmu.2011.00035 (2011). [PubMed: 22566825]
38. Islam S et al. Quantitative single-cell RNA-seq with unique molecular identifiers. Nat Methods 11, 163–166, doi:10.1038/nmeth.2772 (2014). [PubMed: 24363023]
39. Huber W et al. Orchestrating high-throughput genomic analysis with Bioconductor. Nat Methods 12, 115–121, doi:10.1038/nmeth.3252 (2015). [PubMed: 25633503]
40. Wu TD & Nacu S Fast and SNP-tolerant detection of complex variants and splicing in short reads. Bioinformatics 26, 873–881, doi:10.1093/bioinformatics/btq057 (2010). [PubMed: 20147302]
41. Law CW, Chen Y, Shi W & Smyth GK voom: Precision weights unlock linear model analysis tools for RNA-seq read counts. Genome Biol 15, R29, doi:10.1186/gb-2014-15-2-r29 (2014). [PubMed: 24485249]

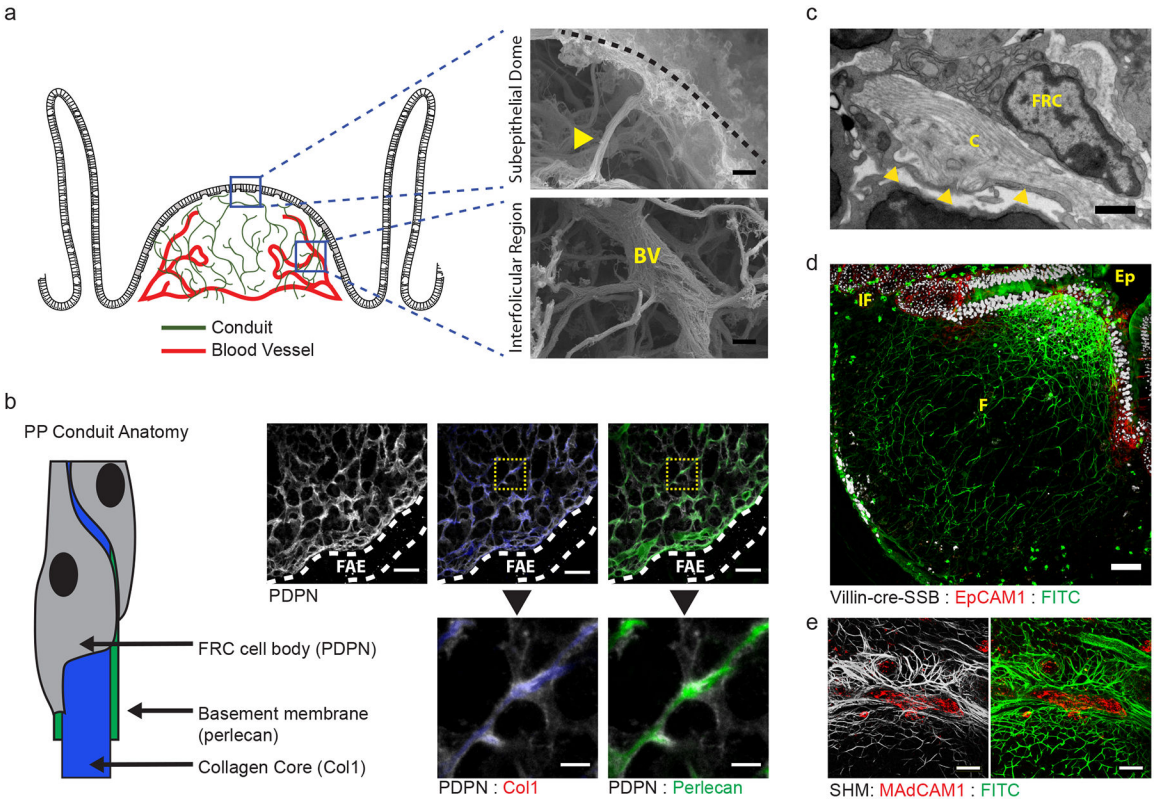

Figure 1. An FRC conduit network facilitates the flow of absorbed lumenal fluids through intestinal PPs.

(**a**) Scanning electron micrograph of PP following alkali-water maceration to remove cells. *top*, PP dome region. Conduit (yellow arrow) extending inward from the ECM underlying the dome epithelium (dashed line). *bottom,* PP interfollicular region. Conduits intersecting a blood vessel (BV) in the PP follicle. Scale bar = 2um. (**b**) Confocal microscopy of the dome region of a PP stained with anti-PDPN, anti-Collagen Type I, and anti-Perlecan. Follicle associated epithelium marked by dotted lines. Scale bar = 20um. Inset Scale bar = 5um. (**c**) Transmission electron micrograph depicting the anatomy of a PP conduit. Basement membrane marked by yellow arrows. Scale bar = 0.5um (**d**) Multiphoton microscopy of a PP from a *Villin*Cre-SSB-BFP mouse after oral gavage with soluble FITC and counterstained with anti-EpCAM1. IF = interfollicular region, F = follicle, Ep = epithelium. Scale bar = 50um (**e**) Multiphoton microscopy of a PP HEV. The mouse was orally gavaged with soluble FITC and the HEV stained by *in vivo* labeling with anti-MAdCAM before perfusion fixation. Data representative of images taken from at least 2 (**a-c**) or 3 (**d,e**) independent experiments.

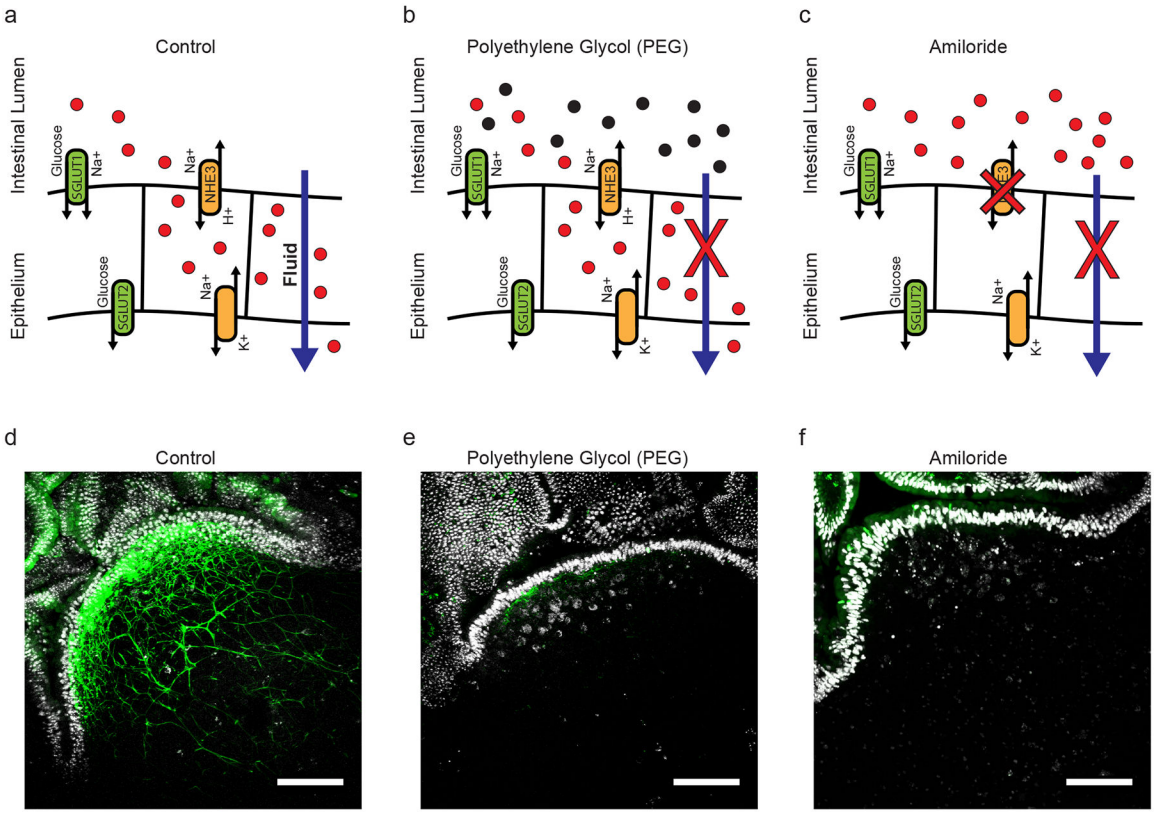

Figure 2. Impaired fluid absorption limits fluid flow into PP conduits.

(**a**) Schematic representation of the establishment of osmotic gradients by Na^+/H^+ transporters in absorptive epithelium. Establishment of this gradient is the primary means of directing fluid uptake. (**b**) Oral delivery of high molecular weight polytheylene glycol (3350 kDa) disrupts the establishment of effective osmotic gradients. PEG is a non-absorbable, non-metabolized, osmotically active agent. (**c**) Amiloride hydrochloride is an inhibitor of the Na^+/H^+ transporters NHE1, NHE2, and NHE3. (**d-f**) Representative images taken by multiphoton microscopy of Peyer's patches from a *Villin*Cre-SSB-BFP mice after oral gavage with soluble FITC in saline (**d**), FITC in PEG (**e**), or FITC in saline+amiloride. Scale bars = 100um. (n=1 PP per mouse, 3 mice per treatment group)

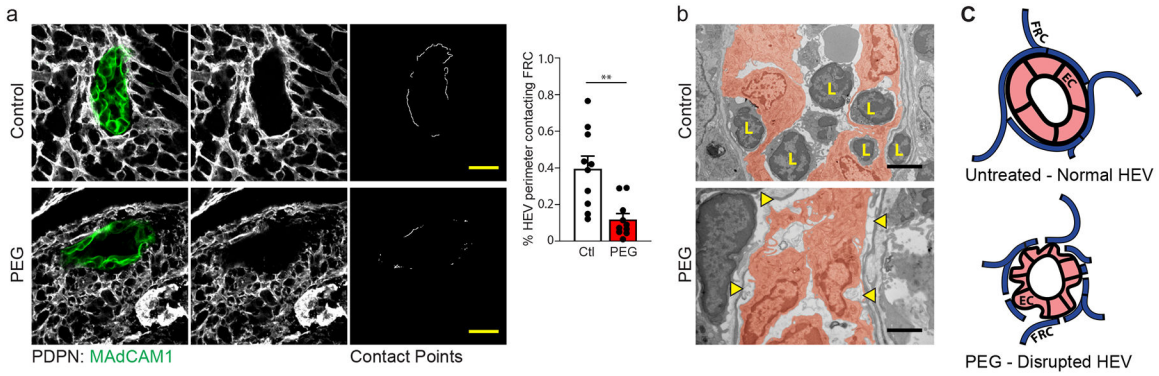

Figure 3. Blockade of fluid absorption alters HEV structure in PPs.

(**a**) Representative images taken by confocal microscopy of an HEV from the PP of an untreated control mouse or a mouse treated for 3 days with PEG in drinking water. *left and middle panels:* HEV ECs and FRCs were marked by staining with anti-MAdCAM1 and anti-PDPN respectively. *right panel:* Contact points between HEV perimeter and surrounding perivascular FRCs. Scale bars = 20um. *Bar graph:* Total quantification of FRC:HEV contact points from confocal imaging. Data represented as mean ± SEM of three independent experiments (n=10 mice per treatment). Unpaired two tailed Student's *t* test was used to compare groups (** $P \leq 0.01$). (**b**) Transmission electron micrograph of PP HEVs. *top panel:* control. *bottom panel:* treated for 3 days with PEG in drinking water. ECs false colored in red. Separations between endothelial cell and basement membrane marked by yellow arrows. Lymphocytes marked by "L". Scale bar = 2um. Representative of two independent experiments. (**c**) Schematic representation of HEV structure in PPs from untreated (upper) and PEG-treated (lower) mice.

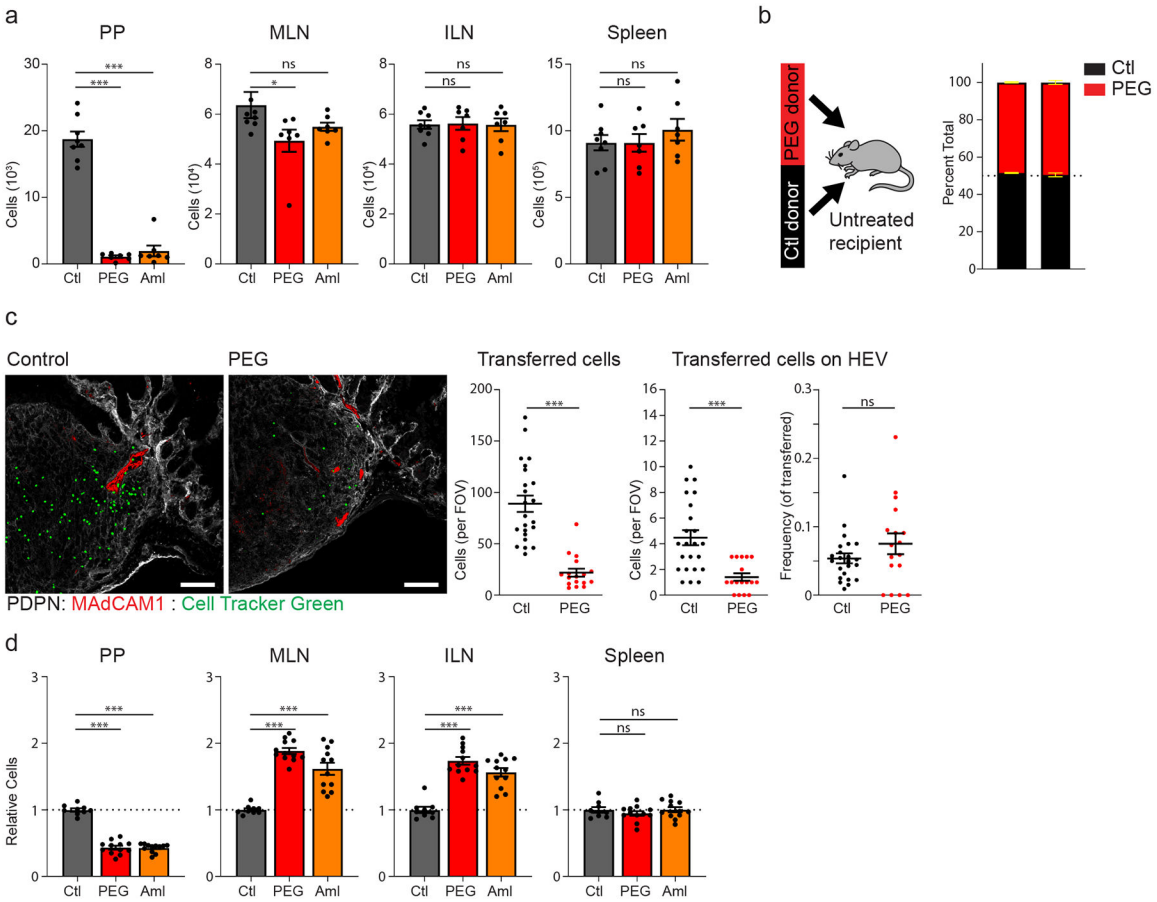

Figure 4. FRC responsiveness to PP conduit fluid flow is necessary to maintain lymphocyte recruitment and PP homeostasis.

(**a**) Flow cytometric analysis of adoptively transferred splenocytes accumulating in the PP, MLN, ILN, and spleen one hour after transfer into control (ctl), PEG-treated (PEG), or amiloride-treated (Aml) recipients. (N = 8 (ctl) or 7 (PEG, aml) mice per group). (**b**) Flow cytometric analysis of adoptively transferred splenocytes accumulating in the PP and LN of an untreated recipient mouse. Adoptively transferred splenocytes were obtained from control and PEG-treated donors and transferred in a 1:1 ratio. (n=5 mice per group). (**c**) Confocal microscopy of PPs from control or PEG-treated recipient mice one hour after adoptive transfer of CellTracker Green-labeled splenocytes. Representative images, co-stained with anti-PDPN (grey) and anti-MAdCAM1 (red). Scale bar = 100um. Quantification of imaging represented as the total number of adoptively transferred cells co-localizing with MAdCAM1$^+$ HEVs (left) or the percentage of adoptively transferred cells co-localizing with MAdCAM1$^+$ HEVs (right). (n=23 (ctl) or n=17 (PEG) PPs, isolated from 5 mice per group). (**d**) Flow cytometric analysis of relative lymphocyte cellularity in the PP, MLN, ILN, or spleen of untreated control (ctl), PEG-treated (PEG), or amiloride treated (Aml) mice. (N = 9 (ctl), 12 (PEG, Aml) mice). For all graphs, data represented as mean ± SEM from three (**a, c, d**) or two (**b**) independent experiments. Groups were compared by one way ANOVA (**a,d**) or unpaired two tailed Student's *t* test (**c**). *P < 0.05, **P < 0.01, ****P < 0.0001. No statistical significance is indicated with "ns"

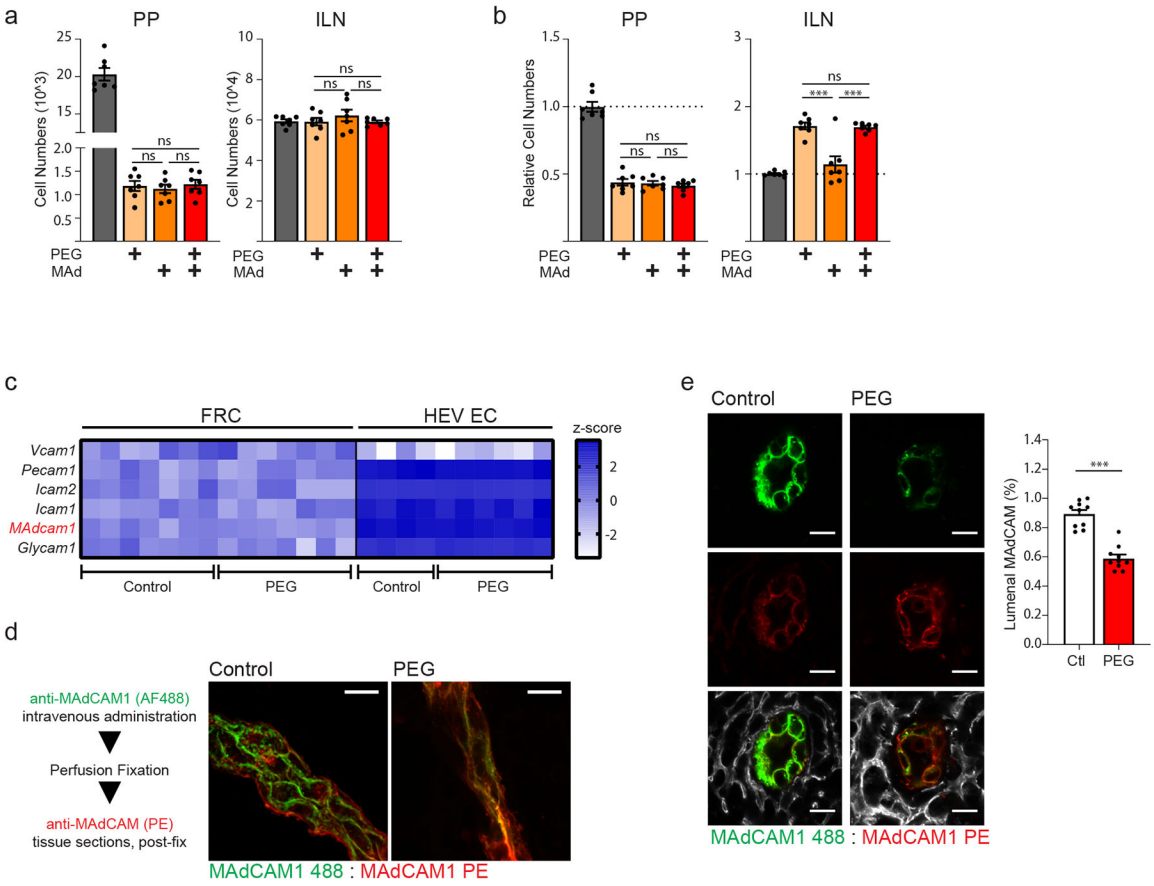

Figure 5. Impaired lymphocyte rolling on HEV and reduced lumenal display of MAdCAM on the HEV surface following loss of PP conduit flow.

(**a,b**) Mice were untreated, treated with PEG, treated by IV injection of anti-MAdCAM, or treated with both PEG and anti-MAdCAM. (n=7 mice per group) (**a**) Accumulation of adoptively transferred lymphocytes to the PP or ILN 1 hour after transfer. (**b**) Total lymphocyte cellularity of the PP and ILN following treatment. (**c**) Expression heat-map of select adhesion molecules involved in lymphocyte recruitment. RNAseq was performed on FACS sorted FRCs and HEV ECs from both control and PEG-treated animals. Data represented as Z-score (n= 7 mice per group (FRC) or 4 mice per group (HEV EC)). (**d,e**) Mice were *in vivo* labeled with anti-MAdCAM in alexafluor 488 by intravenous injection. Mice were perfused with fixative and tissue sections from PPs were re-stained with anti-MAdCAM in PE. (**d**) Confocal microscopy of an HEV (longitudinal orientation) from a control (untreated) and PEG-treated mouse. Representative of three independent experiments (**e**) Representative image taken by confocal microscopy of PP HEVs (cross-sectional orientation) from control and PEG-treated mice Cumulative data is quantified and displayed as percentage of pixels positive in MAdCAM-AF488 out of total MAdCAM$^+$ pixels (% lumenal MAdCAM). Scale bars = 10um. (n=10 mice per group) For all graphs, data represented as mean ± SEM from three independent experiments. Groups were compared by one way ANOVA (**a,b**) or unpaired two tailed Student's *t* test (**e**). *P < 0.05, **P < 0.01, ****P < 0.0001. No statistical significance is indicated with "ns"

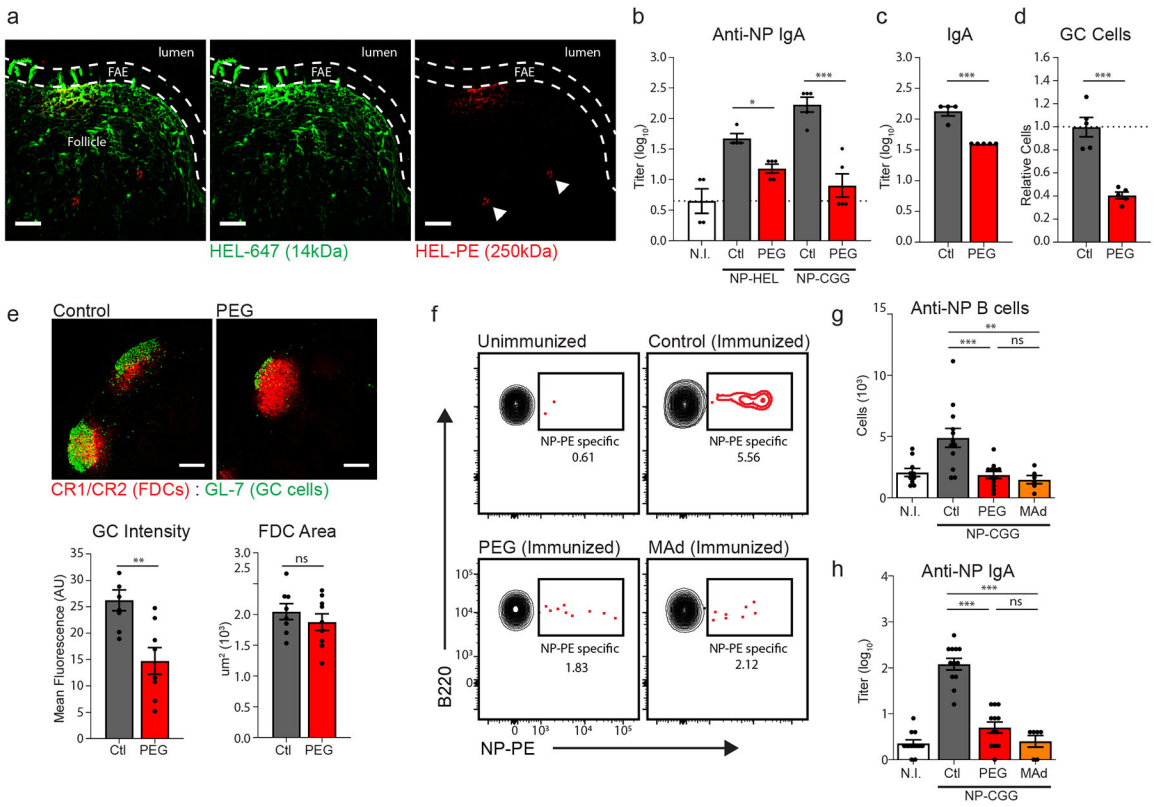

Figure 6. Blockade of fluid absorption impacts mucosal humoral responses.

(**a**) Confocal microscopy of a PP following intralumenal injection HEL-647 and HEL-PEG in explanted intestinal loops. Follicle associated epithelium (FAE) marked by dashed line. Scale bars = 50um. Representative of three independent experiments. (**b**) Anti-NP fecal IgA titers quantified by ELISA. Experiments compare the following treatment groups: normal drinking water and unimmunized (N.I.), normal drinking water and immunized (control, Ctl), PEG-treated and immunized (PEG). Antigens used for immunization were either NP-HEL (14kDa) or NP-CGG (150kDa). (n = 4 (n.i.) or 5 (ctl,PEG) mice per group). (**c-e**) Analysis of baseline humoral immune activity in untreated (ctl) or PEG-treated mice. (**c**) Total fecal IgA titers measured by sandwich ELISA (n = 4 (ctl) or 5 (PEG) mice per group). (**d**) Flow cytometric analysis of GL7+CD38− germinal center cell frequencies in the PP (n=5 mice per group). (**e**) Confocal imaging of germinal center activity. GC cells identified by GL7, FDC network identified by CR1/CR2. GC intensity and FDC network area were quantified in ImageJ. Scale bars = 200um. (n=8 mice per group). (**f-h**) Analysis of NP-specific humoral response following immunization against NP-CGG. Treatment groups include unimmunized (NI), control immunized (ctl), PEG-treated and immunized (PEG), and anti-MAdCAM1 treated and immunized (MAd). (N = 10 (NI), 12 (ctl, PEG), or 6 (MAd) mice) (**f**) Representative flow cytometric analysis of NP-specific B cell numbers in the intestinal lamina propria. (Gated on $CD45^{+}$, $EpCAM^{-}$). (**g**) Quantification of total NP-specific B cell numbers in the intestinal lamina propria. (**h**) Anti-NP fecal IgA titers quantified by ELISA. For all graphs, data represented as mean ± SEM from three (**f-h**) or two (**b-d**) independent experiments. Groups were compared by one way ANOVA (**b,g,h**) or

unpaired two tailed Student's *t* test (**c,d,e**). *P < 0.05, **P < 0.01, ****P < 0.0001. No statistical significance is indicated with "ns"

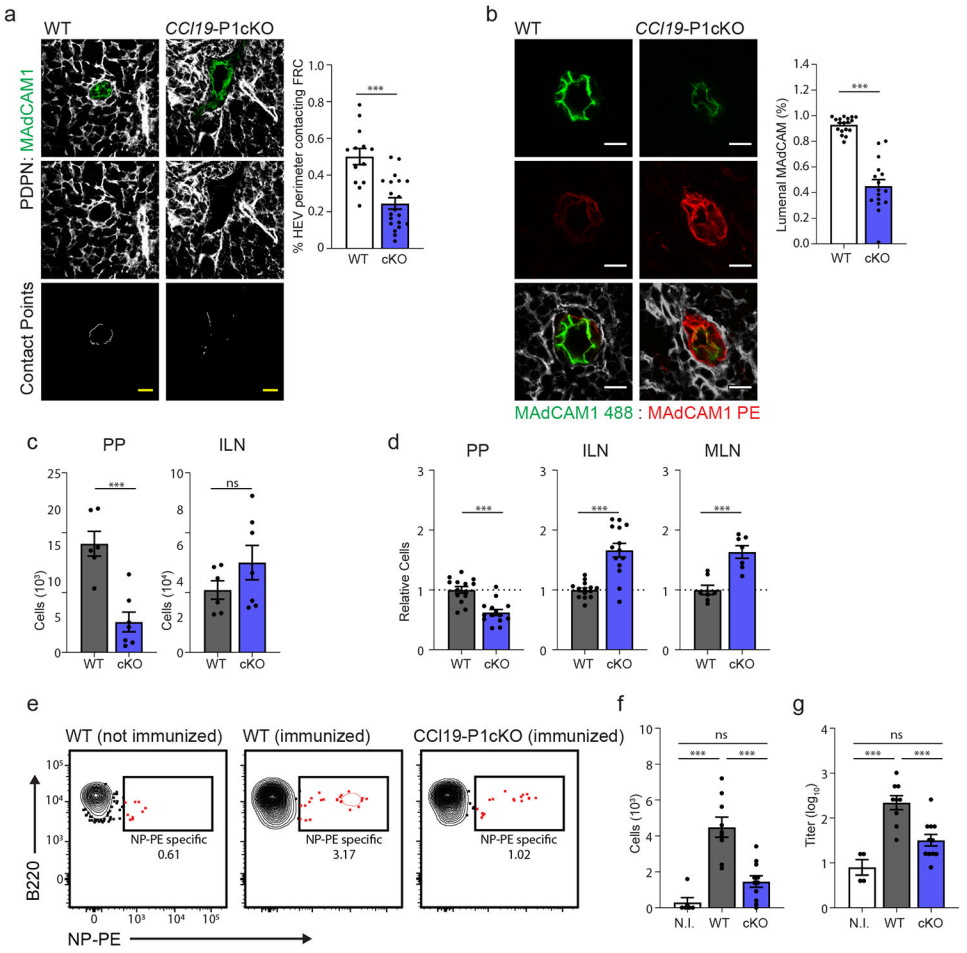

Figure 7. FRCs respond to conduit fluid flow via Piezo1-mediated mechanosensation.

(**a**) Representative images taken confocal microscopy of HEVs from *Ccl19*Cre $^{-}$ × Piezo1$^{fl/fl}$ (WT) and *Ccl19*-P1cKO mice. *top and middle panels:* HEV ECs and FRCs were marked by staining with anti-MAdCAM1 and anti-PDPN respectively. *lower panel:* Contact points between HEV perimeter and surrounding perivascular FRCs. Scale bars = 20um. *Bar graph:* Total quantification of FRC:HEV contact points from confocal imaging (n = 13 (WT) or 17 (cKO) mice). (**b**) Representative images taken by confocal microscopy of PP HEVs (cross-sectional orientation) from *Ccl19*Cre $^{-}$ × Piezo1$^{fl/fl}$ (WT) and *Ccl19*-P1cKO mice. Mice were *in vivo* labeled with anti-MAdCAM in alexafluor 488 by intravenous injection, then perfused with fixative and tissue sections from PPs were re-stained with anti-MAdCAM in PE. Cumulative data is quantified and displayed as percentage of pixels positive in MAdCAM-AF488 out of total MAdCAM^{+} pixels (% lumenal MAdCAM). Scale bars = 10um. (n = 18 (WT) or 16 (cKO) mice) (**c**) Flow cytometric analysis of adoptively transferred splenocytes accumulating in the PP or ILN one hour after transfer into *Ccl19*Cre $^{-}$ × Piezo1$^{fl/fl}$ (WT) and *Ccl19*-P1cKO recipients. (n = 6 (WT) or 7 (cKO) mice) (**d**) Flow cytometric analysis of total lymphocyte cellularity in the PP, ILN, and MLN of *Ccl19*Cre $^{-}$ × Piezo1$^{fl/fl}$ (WT) and *Ccl19*-P1cKO mice. Data are represented as fold change relative to untreated control mice. (n=14 mice per group). (**e-g**) Analysis of NP-specific humoral response following immunization against NP-CGG. Treatment groups include unimmunized

WT mice (NI), immunized *Ccl19*Cre^{-} × Piezo1$^{fl/fl}$ mice (WT), and immunized *Ccl19*-P1cKO mice (cKO). (n = 6 (NI), 9 (WT) or 11 (cKO) mice) (**e**) Representative flow cytometric analysis of NP-specific B cell percentages in the intestinal lamina propria. (Gated on CD45^{+}, EpCAM^{-}). (**f**) Quantification of total NP-specific B cell numbers in the intestinal lamina propria. (**g**) Anti-NP fecal IgA titers quantified by ELISA. For all graphs, data represented as mean ± SEM from at least three independent experiments. Groups were compared by one way ANOVA (**f,g**) or unpaired two tailed Student's *t* test (**a-d**). *P < 0.05, **P < 0.01, ****P < 0.0001. No statistical significance is indicated with "ns"